npj | computational materials

Article

Published in partnership with the Shanghai Institute of Ceramics of the Chinese Academy of Sciences

https://doi.org/10.1038/s41524-026-02334-0

# Resolving kinetics of halide separation in perovskites by polaron-based lattice model and in situ X-ray diffraction

Check for updates

Sebastian Schwartzkopff[1], Ivan Zaluzhnyy[1] ✉, Ekaterina Kneschaurek[1], Dmitry Lapkin[1], Hans Mauser[1], Niels Scheffczyk[1], Paul Zimmermann[1], Alexander Hinderhofer[1], Frederik Unger[1,2,3], Fabian Westermeier[2], Yana Vaynzof[4,5], Fabian Paulus[4] & Frank Schreiber[1] ✉

Light-induced phase separation (LIPS) in mixed lead-halide perovskites is one of the major obstacles to high-efficiency perovskite-based tandem solar cells, yet the mechanisms that govern it remain unclear. Using in situ X-ray diffraction on $MAPbBr_{1.8}I_{1.2}$, we track coexisting phases through their lattice parameters and observe the same kinetics across all samples: phase separation sets in only after a delay, with an iodide-rich phase appearing abruptly at near-pure composition while the residual mixed phase drifts gradually towards bromide. To capture this behaviour, we extend the Kawasaki Hamiltonian, adding separate polaron-induced stress terms for electrons and holes, and evolve the halide lattice by Monte Carlo simulation. The model reproduces both the delay and the asymmetry, neither of which follows from standard Cahn-Hilliard kinetics. Within the model, the stronger coupling of electron polarons in bromide-rich regions dominates the driving force, pointing to electron-phonon coupling as a lever for suppressing LIPS.

Lead-halide perovskites (LHPs) have attracted significant attention, primarily as a prospective material for photovoltaic applications and especially in producing highly efficient, low-cost solar cells[1–3]. Their high efficiency stems from low exciton binding energies as well as large charge carrier diffusion lengths, while the low cost can be maintained by utilising solution-based fabrication techniques at relatively low temperatures[1,4–7]. Unfortunately, LHPs are sensitive structures that can disintegrate under non-ideal conditions such as high moisture, heat, or even illumination[8,9]. Therefore, a comprehensive understanding of these materials is required, which also constitutes a formidable fundamental challenge, to further improve their environmental stability and efficiency.

Pure LHPs follow the formula $ABX_3$, where A is an organic ($CH_3NH_3^+$ – methylammonium (MA), $CH(NH_2)_2^+$ – formamidinium (FA)) or inorganic ($Cs^+$, $Rb^+$) cation filling the voids between the interconnected $BX_6$ octahedra. In LHPs, the B-site is occupied by $Pb^{2+}$, while the X-sites are occupied by halide ions ($I^-$, $Br^-$, or $Cl^-$). Mixing halides within LHPs enables precise band gap tuning across the full range between the two pure compounds, as demonstrated by materials such as $MAPbBr_{1.8}I_{1.2}$[10–12]. This tunability makes mixed-halide LHPs prime candidates for high-efficiency tandem solar cells[13]. However, experiments have shown that under sufficiently intense continuous illumination the mixed phase undergoes phase separation during which the uniform distribution of halide anions becomes disrupted, and domains of bromide-rich and iodide-rich phases are formed[14]. These domains exhibit two distinct band gaps approaching those of the pure compounds. More detrimentally, iodide-rich domains act as charge carrier traps, owing to their lower band gap. Charge carriers are funnelled into these traps where they undergo radiative and non-radiative recombination, thereby significantly reducing device efficiency[14–16]. Notably, the phase separation is largely reversible, with the system returning towards its initial mixed state in the absence of illumination[14], although complete recovery is not always observed and depends on factors such as the sample environment[17].

Various ways to suppress this light-induced phase separation (LIPS) have been investigated. These include additives[18–20], the inclusion of 2D perovskites[21], reducing the number of grain boundaries[22–24], as well as optimising the orientation of crystal grains[25], or tuning the grain size[26–28]. However, the underlying phase separation mechanisms remain elusive. Various theoretical frameworks, including thermodynamic, polaron-induced stress, and redox models, have been proposed to explain these observations[5,29,30], and it is possible that a combination of these mechanisms is responsible for the observed phase separation. An in situ characterisation of the phase separation should therefore provide further insights.

[1]Institut für Angewandte Physik, Universität Tübingen, Tübingen, Germany. [2]Deutsches Elektronen Synchrotron DESY, Hamburg, Germany. [3]Department Physik, Universität Siegen, Siegen, Germany. [4]Leibniz-Institute for Solid State and Materials Research Dresden, Dresden, Germany. [5]Chair for Emerging Electronic Technologies, Technische Universität Dresden, Dresden, Germany. ✉e-mail: ivan.zaluzhnyy@uni-tuebingen.de; frank.schreiber@uni-tuebingen.de

The goal of this work is to understand the length- and time-scales of the phase separation and investigate the evolution of the domains of mixed and separated phases. Commonly, this is done utilising photoluminescence spectroscopy (PL). However, while successful in its own right, the PL signal is dominated by the energetic funnelling of photogenerated charge carriers into iodide-rich minority domains, where they preferentially recombine radiatively[16]. Therefore, the PL signal does not directly reflect the bulk rate or extent of separation[31]. X-ray diffraction (XRD), which probes the whole volume and is independent of optical properties of different phases, does not have these limitations. Therefore, in this work, the phase separation was investigated using in situ XRD, providing a direct and quantitative picture of the phase separation kinetics.

To support the experimental results and gain further insight into the forces driving the phase separation, we performed numerical simulations based on the Kawasaki Hamiltonian extended to include polaron-induced stress[32,33]. This approach reproduces the experimentally observed delay in phase separation after turning on the light, which emerges naturally from the polaron-induced stress, whereas other approaches such as Cahn-Hilliard would have to be modified in non-trivial ways to capture it. In this model, polarons are the primary driving force behind phase separation. Unlike conventional semiconductors, the soft ionic lattice of LHPs undergoes significant local deformation in response to these polarons, inducing internal stress[16,29,34,35]. The system can subsequently reduce this elastic strain energy by undergoing phase separation. Reproducing the measured kinetics in this model requires electron polarons to be the dominant driver of the phase separation. This suggests a possible design principle for suppressing LIPS: mixed-halide compositions with weaker electron-phonon coupling may be inherently more stable under illumination.

## Results

### Bulk-sensitive observation of phase separation by in situ XRD

To track LIPS in real time, we illuminated spin-coated $MAPbBr_{1.8}I_{1.2}$ films with a blue light-emitting diode (LED, $\lambda$ = 450 nm) while probing them in situ by high-resolution XRD ($E$ = 11.85 keV) around the 001 reflection, as shown in Fig. 1 for one representative sample. Figure S3 presents all five measurements, including the representative sample of Figure 1, which show the same qualitative behaviour. Full sample preparation and experimental details are given in the Methods (see Figure S4 for the measurement geometry). The 001 peak of the mixed phase is confined to a narrow range around $q_z$, indicating that the films are well-aligned with grains preferentially oriented out-of-plane. In all samples, the dark-state peak sits marginally above the position expected for the nominal $MAPbBr_{1.8}I_{1.2}$ composition, consistent with a slightly bromide-rich incorporated film (see Supplementary Information). This does not affect the conclusions below, which concern the evolution of the phases rather than their absolute starting composition.

Within the first few seconds after switching on the LED at $t$ = 0 min, this peak broadens, most likely driven by polaron-induced lattice stress, a known source of effective peak broadening[36,37]. The resulting asymmetric peak profile cannot be accurately captured by a single Voigt function (see Figure S2). Specifically, the tail at lower $q$ has, on average, twice the integrated intensity of the one at higher $q$, indicating that lattice expansion affects a larger crystalline volume fraction than compression under polaron-induced stress.

The initially broadened peak slowly narrows again, pointing towards the lattice reducing the light-induced internal stress through halide redistribution, thereby marking the onset of phase separation. During this time, the temperature of the LHP layer increases due to photothermal dissipation. This causes a lattice expansion and a shift of the diffraction peak towards lower $q$-values by an average of 5.94(53) $\times 10^{-4}$ Å$^{-1}$ (mean, s.d. over five samples). Assuming purely thermal expansion, the observed lattice expansion corresponds to a temperature increase of approximately 7 K under LED illumination, based on a thermal expansion coefficient of 7.9 $\times 10^{-5}$ K$^{-1}$ determined independently for the same samples. The estimated 7 K thermal rise is sufficient to account for the observed shift. Additionally,

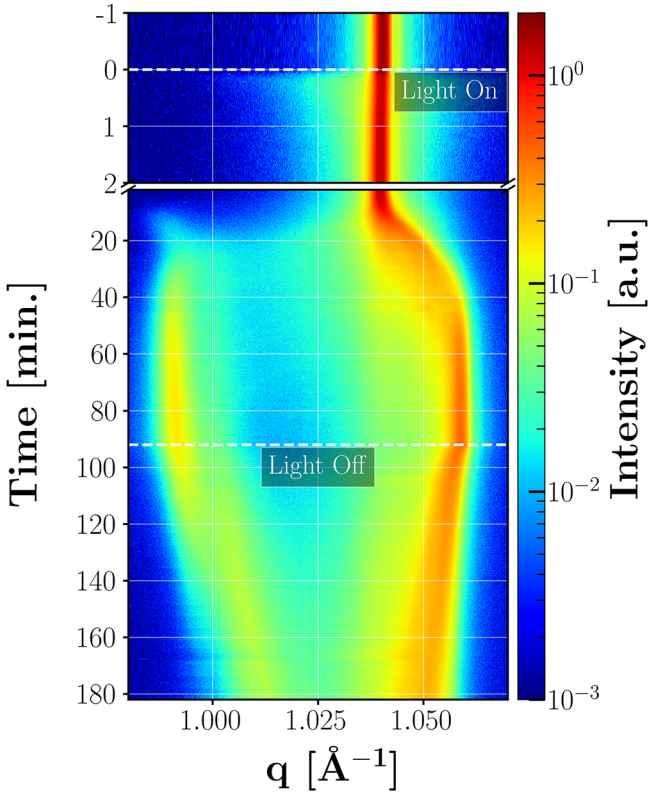



**Fig. 1 | Temporal evolution of the 001 peak in $q$-space during phase separation of $MAPbBr_{1.8}I_{1.2}$.** The peak is azimuthally integrated over the narrow range of about 12° covered by the detector. The time axis starts at $t$ = −1 min, i.e., one minute of dark before the LED was turned on at $t$ = 0 min to trigger the phase separation (upper white dotted line). After $t$ = 2 min, the temporal resolution of the plot is decreased, indicated by a white gap at $t$ = 2 min, to show the long-term evolution of the scattering signal, while also highlighting initial short-term changes. After $t$ = 92 min the LED was turned off to allow for remixing (lower white dotted line).

photoinduced lattice expansion has been reported in halide perovskites under above-band gap illumination[37–39], as is the case here, and a contribution from this effect cannot therefore be excluded.

As the local halide composition evolves during LIPS, the local lattice parameter changes in response, making the phase separation increasingly apparent in the diffraction pattern. This results in a broadening and splitting of the diffraction peak into two components: an iodide-rich peak appearing at its final position at $q \approx 0.99$ Å$^{-1}$ (consistent with pure tetragonal $MAPbI_3$) without any measurable gradual shift, and a bromide-rich component shifting continuously towards $q \approx 1.06$ Å$^{-1}$ (consistent with pure cubic $MAPbBr_3$). Since Vegard's law provides a good local approximation of the relationship between lattice parameter and halide composition[40], the peak position can be used as a proxy for composition. This indicates that iodide rapidly falls out of the mixed phase and accumulates directly into a near-pure $MAPbI_3$ phase, while the remaining mixed phase gradually transitions into a bromide-rich phase. This asymmetry points towards a stronger driving force for iodide separation, a key kinetic feature we return to in the Discussion.

In all samples, we observe the appearance of a Bragg peak which aligns with the 001 peak position of $MAPbI_3$. Owing to the tetragonal structure of the iodide phase, the 001 reflection is expected to split into a $c$-axis component at 0.99 Å$^{-1}$ and an $a$/$b$-axis component at 1.0 Å$^{-1}$. Since the grains are preferentially oriented out of plane, the measurement along $q_z$ probes mainly the out-of-plane lattice spacing, and we predominantly observe the $c$-axis component. This indicates that the longer $c$-axis is oriented perpendicular to the substrate surface. The $a$/$b$-axis is then most likely oriented in-plane, although we cannot confirm this directly, as the corresponding 100/

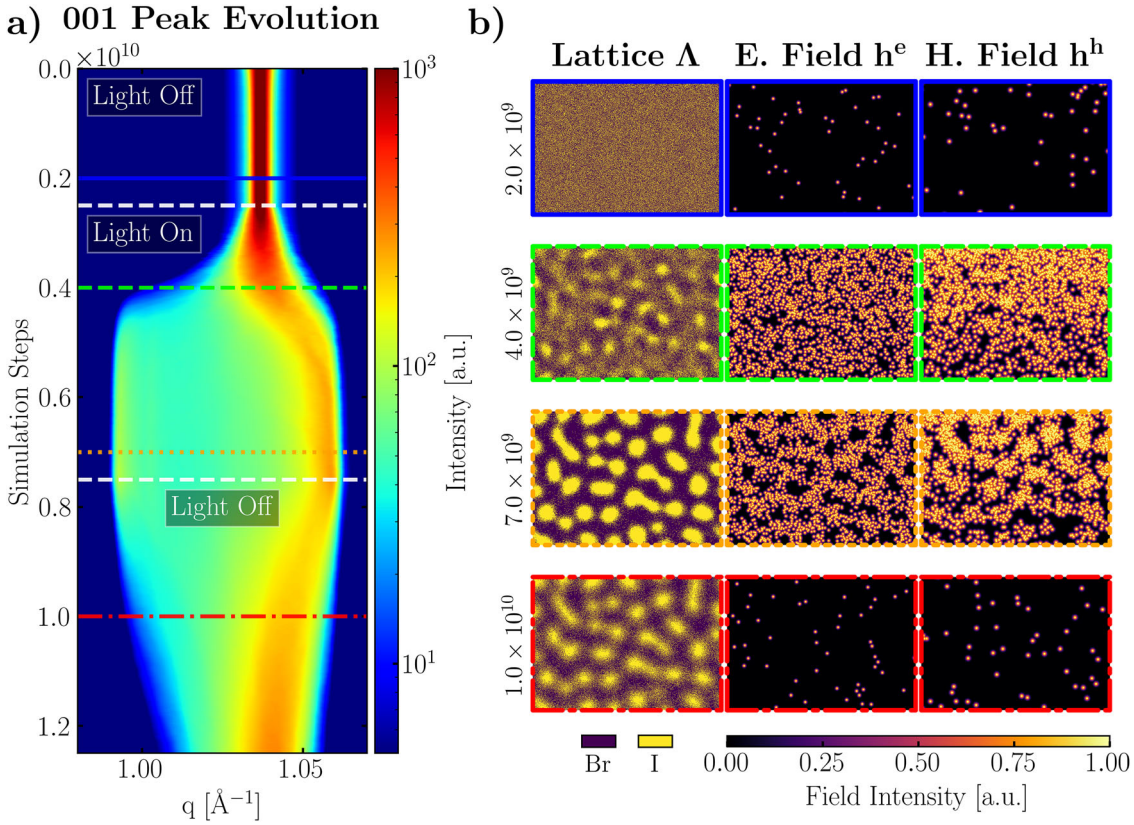



**Fig. 2 | Example of the simulated phase separation (see Table 1 for simulation parameters). a** Evolution of the 001 diffraction peak for the simulated phase separation. **b** The halide sublattice $\Lambda$ (entries +1: iodide, −1: bromide), as well as the electron- and hole-polaron fields $h^e$ and $h^h$ (polaron field strength at each lattice site), are shown for different time steps; see Methods for details. The selected time steps are marked on the 001 peak evolution shown in panel (a). The number of simulation steps is shown to the left of each row. Only the lower half of the halide lattice $\Lambda$ is shown, corresponding to one physical film with the illuminated surface at the top and the light decaying into the film (see Methods).

010 reflections were not observed. This orientation is favoured because in-plane expansion is suppressed by neighbouring grains, while the out-of-plane direction allows the lattice to expand more readily.

Although the main features of LIPS are well reproducible, the samples shown in Figure S3 are not identical, which results in some deviations in separation rate and stability of the original phase. In some cases (Figure S3c) the mixed phase remains present for almost all 92 minutes of illumination, while in others it quickly demixes within roughly 60 minutes (Figure S3e). Ultimately, most of the samples (a, d, and e) underwent a nearly full phase separation by the end of the illumination period. The origins of this sample-to-sample variation are most likely related to differences in defect density and crystallinity, which influence the mobility of ions and polarons. Other factors, such as the sample thickness and the illumination geometry (LED alignment and LED-to-sample distance), may have a smaller influence on the LIPS (see Supplementary Information).

After turning off the light at $t = 92$ min, both peaks slowly move back together towards $q_{001} = 1.04$ Å$^{-1}$, indicating remixing. During this process, a jump in the iodide-rich peak appears near $q \approx 1.0$ Å$^{-1}$, consistent with the iodide-rich phase reverting from its tetragonal structure to the cubic structure of the mixed phase as its iodide content decreases. However, none of the samples fully recovered after 90 min of dark, with remixing proceeding more slowly than phase separation. Nonetheless, the remixing rate is comparable across samples.

### Monte Carlo simulation of polaron-driven phase separation

To gain deeper insights into the light-induced halide dynamics, we performed Monte Carlo simulations using the polaron-induced stress model based on the Kawasaki Hamiltonian (see Eq. (4), Methods and Supplementary Information for details). In the model, the halide sublattice is represented by a two-dimensional grid of iodide and bromide sites that evolves through Monte Carlo nearest-neighbour swaps, where illumination generates polarons that locally strain the lattice and thereby favour demixing. At each step the configuration is converted into a simulated 001 diffraction peak, allowing direct comparison with the measured evolution. The results of the simulation are shown in Fig. 2.

When the light is switched on, modelled by raising the number of polarons, the original diffraction peak drifts towards the pure-bromide position and an iodide-rich peak emerges on a timescale consistent with the experimental observations. To reproduce this timescale, several parameters were iteratively optimised, while others were fixed from measurements, theory, or literature (see Methods and Supplementary Information). The delayed onset of phase separation, however, follows from the model itself rather than from this tuning. When the light is switched off, modelled by reducing the polaron count to its low dark-state value, the two peaks remix at a slower rate. The simulation additionally reproduces the absence of phase separation at low illumination (see Figure S7), consistent with the samples showing no signs of prior phase separation in the initial dark-state measurements, despite brief exposure to ambient light during sample mounting. Furthermore, the simulations predict that phase separation is inhibited at very high polaron densities (see Figure S7). This result is consistent with the experimental observations by Mao et al.[33], who reported that high carrier densities can stabilise the mixed-halide phase. It should be noted, however, that other experimental behaviours have also been reported, including saturation of the separation rate at high illumination intensities[41] and an increase in the separation rate with increasing illumination intensity at temperatures below 300 K[42].

Figure 2b shows the corresponding real-space evolution at the four time steps marked in Figure 2a. In the dark, mixed state (row 1) the halide

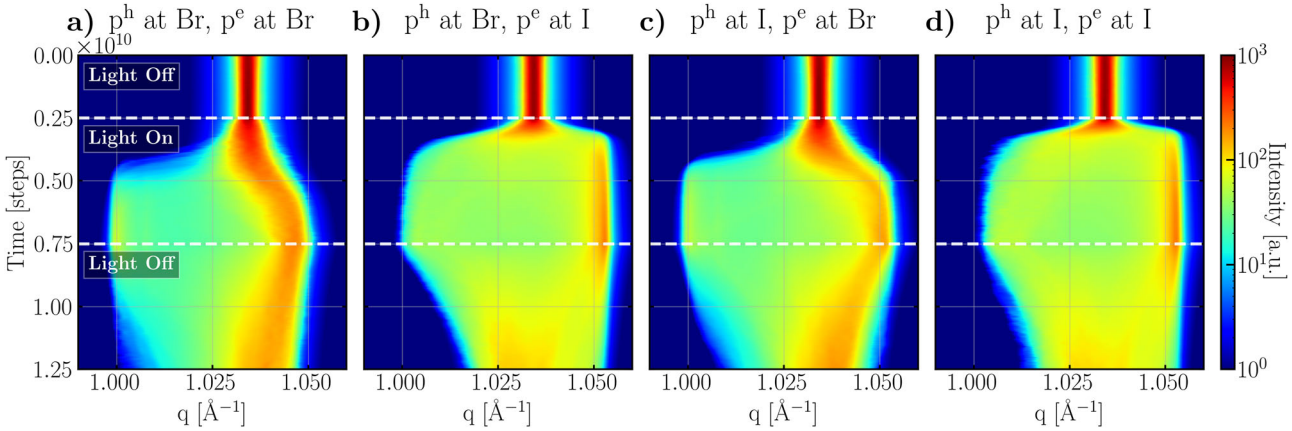



**Fig. 3 | Comparison of different distributions of hole- ($p^h$) and electron-polarons ($p^e$) using simulation parameters from Table 1.** Each panel shows the time evolution of the 001 diffraction peak during illumination and recovery in the dark. Only the halide species at which the polarons accumulate were varied between bromide (Br) and iodide (I). **a** Both polaron species accumulate within bromide-rich regions. **b** Holes accumulate within bromide-, electrons within iodide-rich regions. **c** Holes accumulate within iodide-, electrons within bromide-rich regions. **d** Both accumulate within iodide-rich regions.

sublattice $\Lambda$ is homogeneously mixed, and only a small number of polarons are present. Under illumination, the polaron count rises, and iodide-rich domains nucleate and grow (rows 2 and 3). The hole-polaron field $h^h$ localises within the iodide-rich regions, while the electron-polaron field $h^e$ localises within the bromide-rich regions, reflecting the polaron-halide coupling that drives the separation. After the light is switched off (row 4) the polaron density returns to its dark value and the domains begin to remix.

An important feature of this model is the presence of random fluctuations in the polaron density. Slow halide migration first allows local halide concentration to drift in response to these fluctuations; once the local halide concentration increases sufficiently, polaron accumulation becomes more likely in that region, which further increases the halide concentration. This positive feedback loop produces phase separation kinetics that are initially slow and accelerate over time, thereby providing a natural delay mechanism consistent with our experimental observations (Figure 1).

The initial broadening observed at the beginning of the illumination is missing in our simulation as we do not model peak broadening due to stress or other effects. Similarly, the faint jump seen experimentally during remixing, which we attribute to the tetragonal-to-cubic transition of the iodide-rich phase, is not reproduced. The concentration-to-$q$ mapping (described in Methods) is interpolated from the available literature lattice parameters[43], whose composition spacing near this structural transition is too large to capture the abrupt change. A mapping that resolved the transition would recover the feature.

Additionally, we systematically tested all four combinations of polaron distribution, in which electron- and hole-polarons can each accumulate preferentially at either iodide- or bromide-rich regions (Fig. 3). Across all four combinations, the same pattern appears: the phase favoured by the more strongly interacting polaron species enriches gradually, producing a continuously shifting diffraction peak, while the complementary phase appears abruptly at its near-pure position. Since reproducing the data requires the electron-polaron interaction to be appreciably stronger than that of the hole, the electron location sets which phase shifts smoothly. Electrons in bromide-rich regions (Figure 3a, c) therefore reproduce the experimental signature of a gradually shifting bromide-rich peak and an abruptly appearing iodide-rich peak, irrespective of the hole location, whereas electrons in iodide-rich regions (Figure 3b, d) produce the opposite behaviour and are inconsistent with the measurements. The physical plausibility of the two matching configurations is discussed in the next section.

## Discussion

A key observation of this study is the appearance of the iodide-rich diffraction peak immediately at its final lattice parameter without any detectable gradual shift towards lower $q$ over time. This suggests that the light-induced migration of iodide leads to the formation of seeds of near-pure $MAPbI_3$ phase, with the peak intensity growing as more material converts into this phase, rather than the gradual increase of iodide concentration in some crystal grains, which would lead to a drift of the diffraction peak position. In contrast, the diffraction peak corresponding to the bromide-rich phase slowly shifts towards higher $q$-values as the bromide concentration increases with time in some domains. To the best of our knowledge, this has not been reported in XRD studies of LIPS. Earlier work either relied on static before/after comparisons[14], which cannot distinguish a sudden compositional jump from a slow drift, or did not address the evolution of the peak position specifically. The absence of a gradual $q$-shift may have gone unnoticed in earlier studies, as PL measurements do not accurately represent the structural evolution of the whole volume[31], and most XRD studies have focused on the extent rather than the compositional trajectory of phase separation.

This absence does not by itself exclude transient intermediate compositions. A newly formed phase only becomes visible in the diffraction pattern once it occupies a sufficient volume fraction, and small domains additionally broaden the reflection, further reducing it relative to the background. Any compositional evolution occurring while the iodide-rich phase is still below this threshold would therefore remain undetected, as would a composition persisting for less than the 12 s between frames at this stage of the measurement. Whether such intermediate states exist could be addressed by measurements with higher time resolution and sensitivity, for instance by faster acquisition on fresh sample positions or by probing individual domains with a nanofocused X-ray beam. The asymmetry itself is unaffected, as the bromide-rich phase continues to shift over tens of minutes, far beyond the resolution of the present measurement.

The observed evolution is inconsistent with a standard Cahn-Hilliard framework or unmodified Kawasaki dynamics[32,44], in which the composition is expected to evolve continuously across the separating phases. Furthermore, both contain no mechanism to reproduce the delayed onset of phase separation observed here, which arises from halides slowly accumulating within a stochastically fluctuating polaron field before polaron localisation sets in. The Monte Carlo approach based on the Kawasaki Hamiltonian naturally accommodates this delay and was therefore preferred.

Beyond these kinetic features, we also observe sample-to-sample variability in the rate and extent of phase separation. We speculate that these differences arise mainly from variations in defect density and crystallinity, which affect intra-lattice diffusion rates and thereby accelerate or slow phase separation, together with variations in sample thickness, which change the fraction of the film that is exposed to a reduced light intensity due to

absorption in the layers above. Variations in the illumination geometry, such as LED alignment or LED-sample distance, change the incident intensity only slightly. This has only a minor effect on the phase separation, as demonstrated in Figure S7. The thickness-dependent behaviour arises because the incident light intensity is attenuated exponentially within the film. With an absorption length of $1/\alpha \approx 46$ nm, which is well below the film thickness of 213 nm for the representative sample, 99% of the LED light is absorbed within the bulk (Figure S1, see Supplementary Information). The photoexcitation density therefore decreases rapidly towards the bottom of the film. Consequently, the top region remains strongly illuminated and undergoes phase separation comparable to that observed in thinner or more uniformly illuminated samples. In the bottom of the film, the polaron density may be significantly lower or even below the phase separation threshold, resulting in a larger amount of mixed phase remaining. Therefore, we observe a comparable phase separation speed while the amount of mixed phase at the end of the illumination can vary. The influence of sample thickness (Figure S5), polaron gradient (Figure S6), and total polaron number (Figure S7) on the simulated extent of phase separation is discussed further in the Supplementary Information.

With the onset of illumination, asymmetric peak broadening is observed (Figure S2), consistent with an early build-up of polaron-induced stress[36]. The subsequent reduction in broadening after a few minutes suggests that the lattice partially relaxes this stress, indicating the onset of phase separation[16,29]. Once both phases coexist within the same crystalline volume, the lattice-parameter mismatch between the pure iodide ($a_I = 6.3$ Å) and bromide ($a_{Br} = 5.9$ Å) phases[43] introduces a misfit strain. As noted above, the tetragonal iodide 001 reflection splits into a *c*-axis and an *a*/*b*-axis component, and we observe predominantly the *c*-axis component along $q_z$, indicating that the longer *c*-axis is oriented out of plane. This orientation relieves the misfit strain, since out-of-plane expansion avoids the in-plane confinement imposed by neighbouring grains.

Under illumination, the lattice responds in two distinct ways. The 001 peak shifts on average, which is accounted for by photothermal heating; a photoinduced lattice expansion may add to this shift, although both its existence and its origin remain debated, with electronic and purely thermal explanations having been put forward[38,39]. In either case, the lattice expands uniformly, so that this contribution bears on the rate rather than the direction of the redistribution. In addition, the polaron-induced stress discussed above deforms the lattice locally and is the only composition-dependent contribution in our model. Temperature enters the model solely through the acceptance criterion of Eq. (2), where it acts on all swaps alike and does not distinguish between the halide species, and cannot by itself produce a compositional asymmetry. Raising $T$ increases the rate at which the barrier $E_B$ is overcome and reduces the relative weight of energy-lowering swaps, the latter favouring mixing rather than separation. In line with this, a further increase in temperature has been reported to slow the separation and to promote remixing through entropic contributions[42]. Within our model, we therefore attribute the observed compositional asymmetry to the polaron-induced stress, while heating and the accompanying lattice expansion affect the rate at which it proceeds.

The slower recovery relative to separation is consistent with this picture. The strain accompanying the light-induced lattice expansion is expected to lower the activation barrier for halide migration under illumination[45], thereby facilitating ion redistribution during separation relative to recovery in the dark. To quantify the effect of the estimated heating within the model, we increased $T$ by 2.3 %, corresponding to a temperature increase in the experiment by 7 K relative to room temperature (Figure S8), which produces only a modest slowdown of the phase separation per Monte Carlo step while preserving the qualitative separation pathway. In real time, the higher temperature also accelerates ion hopping, partially offsetting this slowdown. However, since the model does not map Monte Carlo steps to an absolute timescale, Figure S8 demonstrates the robustness of the separation mechanism rather than the absolute kinetics.

These experimental features are captured by the presented Monte Carlo simulation framework, which employs the previously proposed polaron-induced stress model[33]. This provides further evidence that electron and hole polarons play a central role in the observed LIPS. Of the four tested polaron configurations in Figure 3, only two can capture the experimentally observed phase separation. The first, in which both electrons and holes accumulate within bromide-rich regions (see Figure 3a), is physically unlikely. The reported band positions of the pure phases[10] place the valence band maximum of the iodide-rich phase roughly 0.7 eV above that of the bromide-rich phase, so holes are strongly funnelled into iodide-rich domains, consistent with the predominantly radiative recombination observed there[16,46]. The conduction band minima, by contrast, differ by only about 0.1 eV, so the electron location is set not by the band alignment but by the polaron-induced stress, which in our model favours the bromide-rich phase. The remaining physically consistent configuration therefore places holes in iodide-rich and electrons in bromide-rich regions (see Figure 3c). The same offsets would also be consistent with both carriers residing in the iodide-rich phase (Figure 3d), but this configuration does not reproduce the measured evolution and is therefore inconsistent with the data.

Furthermore, reproducing the data requires the electron-polaron interaction to be substantially stronger than that of the hole ($c_h = 20$, $c_e = -75$), although the precise ratio is less constrained, suggesting that electron polarons provide the dominant contribution to the phase-separation driving force within this model. Since $c_e$ represents the electron-polaron stress coupling, whose magnitude reflects the strength of the Fröhlich electron-phonon interaction[34], a weaker electron-phonon coupling yields a smaller driving force for phase separation.

The model is a minimal kinetic framework by design. It utilises a 2D sublattice that evolves through direct nearest-neighbour swaps rather than explicit vacancy-mediated diffusion and does not incorporate grain boundaries or three-dimensional elastic interactions, while the polaron distribution is assumed to follow the local halide concentration. These simplifications limit how directly the microscopic origin of the asymmetry, and the assignment of specific carrier species can be mapped onto the real material. Mechanisms such as defect-assisted ion migration are not captured by the model and may still contribute.

In summary, in situ XRD resolves the compositional trajectory of light-induced phase separation in mixed-halide perovskites with a bulk sensitivity and time resolution beyond the reach of PL, revealing that the iodide-rich phase forms abruptly at near-pure composition, while the residual mixed phase enriches gradually in bromide. A Monte Carlo model that resolves the polaron-induced stress into separate electron and hole contributions reproduces this asymmetry together with the delayed onset of separation, neither of which follows from the continuous demixing of standard Cahn-Hilliard dynamics, and, within the model, attributes the dominant driving force to electron polarons in bromide-rich regions. Weaker electron-phonon coupling therefore emerges as a candidate design principle for suppressing LIPS, a route towards stable, high-efficiency perovskite-based tandem photovoltaics.

## Methods

We chose MA-based LHPs with a Br:I ratio of 3:2, as this composition is known to exhibit reliable and relatively fast phase separation under illumination[47], making it well-suited for time-resolved in situ XRD experiments. In this study, the composition $MAPbBr_{1.8}I_{1.2}$ refers to the nominal precursor ratio; the incorporated film is slightly more bromide-rich, as discussed in the Supplementary Information.

### Sample preparation

To produce the samples, we followed a previously reported procedure[48–50]. Methylammonium iodide (Greatcell Solar) and methylammonium bromide (Greatcell Solar) were each dissolved separately in anhydrous dimethylformamide (DMF, Sigma-Aldrich) at a concentration of 2.206 mmol/mL. The two solutions were then mixed to achieve a methylammonium halide (MAX) solution with a bromide:iodide ratio of 3:2. Next, hypophosphorous acid (HPA, 50% in water, Sigma-Aldrich; 1.6 $\mu$L HPA per 100 mmol of halide) was added to the solution. Finally, the solution was

combined with lead acetate trihydrate (99.999%) to yield a halide:lead ratio of 3:1.

Precut 12 mm × 12 mm glass substrates (0.7 mm thick) were cleaned in a sonication bath for 10 min with ethyl acetate, acetone, and 2-propanol (all Sigma-Aldrich). Afterwards, they were dried with nitrogen and plasma treated with oxygen at 0.4 mbar and 100 W for 10 min. They were then stored in a humidity-controlled dry box, with a relative humidity <1%. The perovskite films were then deposited by spin-coating the precursor solution onto these substrates at 2000 rpm for 60 s, followed by drying with a mild flow of compressed air for 20 s. Afterwards, they rested in the dry box for 5 min followed by thermal annealing for 5 min at 100 °C. For transportation, samples were stored in the dark in a sealed nitrogen container.

### Experimental Setup

The experiments were conducted at the Coherence Applications beamline P10 of the PETRA III storage ring (DESY, Hamburg). Throughout the measurement, the samples were held in a dry $N_2$ atmosphere (see Figure S4). This environment was chosen to suppress oxygen- and moisture-related changes to the film during the measurement, while also keeping the phase separation reversible[17]. We illuminated the samples for 92 min using a blue light-emitting diode (LED) from Thorlabs (wavelength $\lambda = 450$ nm), providing a continuous illumination power density of approximately 0.45 W/cm$^2$ at the sample's surface (roughly four suns illumination). The illuminated area was a square of 1.5 cm ×1.5 cm, larger than the substrate, so that the entire film was illuminated at approximately uniform intensity. The X-ray footprint lay well within the illuminated region. The LED wavelength was chosen to provide above-band gap excitation for both the mixed phase ($h\nu = 2.75$ eV, $E_{\mathrm{gap,mixed}} = 1.96$ eV) and the pure halide end members ($E_{\mathrm{gap,I}} = 1.59$ eV, $E_{\mathrm{gap,Br}} = 2.30$ eV)[10], ensuring free charge carrier generation throughout the phase separation. This illumination period was followed by 90 minutes of recovery in the dark with the LED switched off.

To track the evolution of the phase separation, we employed in situ, time-resolved X-ray diffraction[31,37,47,51,52]. Measurements were performed using an X-ray beam with an energy of $E = 11.85$ keV ($\lambda = 1.046$ Å). This allowed us to observe changes in the lattice parameters, which are directly connected to halide concentration via Vegard's law[40,53]. The 2D images of the pseudo-cubic 001 peak at $q = 0.99$ –1.06 Å$^{-1}$ were recorded by an Eiger X 4M detector positioned 5 m downstream from the sample at $2\theta = 9.7^{\circ}$ in reflection scattering geometry (see Figure S4). The large sample-to-detector distance ensures a high resolution in reciprocal space needed to track the splitting of the 001 peak during the phase separation. The detector position was chosen such that the reflections of pure tetragonal $MAPbI_3$ (at 0.99 Å$^{-1}$ and 1.0 Å$^{-1}$) and cubic $MAPbBr_3$ (at 1.06 Å$^{-1}$) fell within the detector range. The X-ray beam was focused to a spot of 7 $\mu$m × 15 $\mu$m (vertical × horizontal) with a footprint of 83 $\mu$m × 15 $\mu$m and a flux of ~$10^9$ photons/s. At this X-ray flux, no indication of radiation damage was observed.

The linear thermal expansion coefficient of $MAPbBr_{1.8}I_{1.2}$ was determined for the samples from the temperature-dependent shift of the 001 peak maximum, measured at eleven temperatures between 293 K and 400 K without illumination.

For each sample, we measured 10 diffraction patterns every 6 s with 1 s exposure time in the dark, followed by 60 diffraction patterns every 2 s with 1 s exposure time during the early illumination period, directly after switching on the light. This measurement period covered the first 2 minutes of illumination, after which the LED remained on for an additional 90 minutes, giving a total illumination time of 92 min. This was followed by another 90 min with the light switched off to investigate the recovery. During each of these 90-min periods, 450 diffraction patterns were collected every 12 s with 1 s exposure time for a total of 900 diffraction patterns. This approach allowed us to capture rapid changes during the first few minutes of the illumination, while still capturing long-term processes without exceeding the radiation damage threshold.

The 2D detector images were subsequently transformed into $q$-space and azimuthally integrated using `pygid`[54]. The resulting intensity evolution in $q$-space $I(|q|)$ was normalised by the current in the storage ring and visualised as a waterfall plot, as seen in Figure 1.

### Simulations

To simulate the time evolution of the scattering signal during halide separation, we modelled the movement of halide species within the perovskite sublattice. The system was simplified by only considering iodide and bromide lattice sites. Nearest-neighbour swaps between these iodide and bromide sites drive the lattice towards configurations that minimise the system's energy, thereby leading to phase separation.

Halide migration in LHPs is known to be driven primarily by vacancy-mediated hopping[55]. For simplicity, and following the approach of Mao et al.[33], the simulation instead employs a direct nearest-neighbour swapping scheme, which conserves local composition and reproduces the correct diffusive statistics without explicitly tracking vacancies.

To reduce computational cost, we simplified the simulations by considering a 2D sublattice for halide species (Fig. 4a, b). The lattice was treated as a matrix $\Lambda$ with entries of $+1$ and $-1$ corresponding to iodide and bromide, respectively (Figure 4b). It was then evolved in time using a Monte Carlo simulation framework. The resulting lattice evolution was convolved with a 2D Gaussian kernel with variance $\sigma_c^2$ to obtain a matrix $C_I$ representing the coarse-grained iodide concentration averaged over several unit cells (Figure 4c, d):

$$C_I(x, y) = \frac{\Lambda(x, y) + 1}{2} * \frac{1}{2\pi\sigma_c^2} \exp\left(-\frac{x^2 + y^2}{2\sigma_c^2}\right), \tag{1}$$

where the asterisk (*) denotes a 2D convolution, while $x$ and $y$ are the lattice coordinates. The width $\sigma_c$ takes the value $\sigma_{c,q}$ for the concentration-to-$q$ mapping and $\sigma_{c,p}$ for the polaron-field generation described below.

Since the iodide concentration $c$ in $MAPb(I_cBr_{1-c})_3$ is directly linked to the lattice parameter, and therefore to the $q$-position of the 001 diffraction peak, one can convert the concentration matrix $C_I$ into a simulated scattering signal. The relationship between $c$ and the corresponding $q$-values was derived from literature values[43] with preprocessing described in the Supplementary Information (Figure 4e). To perform this conversion, $C_I$ is computed using Eq. (1) with the standard deviation $\sigma_{c,q}$. This parameter sets the spatial range over which the local lattice parameter adjusts in response to the surrounding halide composition. Each element of $C_I(x, y)$ is then converted to the corresponding $q$-position of the 001 diffraction peak, and the resulting values are binned into a histogram (Figure 4f) to obtain the ideal scattering signal. Repeating this procedure for every time step allows us to track the evolution of the Bragg peak during phase separation and remixing.

The experimentally measured diffraction peak is broadened by a combination of instrumental contributions and sample effects, including inhomogeneous strain and finite grain size[36]. To take these effects into account, we blurred the histogram using a 1D Voigt kernel. The Voigt parameters were matched to the measured dark-state peak shape, yielding $\sigma = 6.9 \times 10^{-4}$ Å$^{-1}$ and $\gamma = 3.2 \times 10^{-4}$ Å$^{-1}$ (with $\sigma$ denoting the standard deviation of the Gaussian component and $\gamma$ denoting the half-width at half-maximum of the Lorentzian component). Finally, all broadened histograms, recorded at successive simulation time steps, are combined into a single matrix representing the evolution of the 001 peak over the course of the simulation (Figure 4g).

The underlying Monte Carlo simulation was based on a modified version of the procedure published by Mao et al.[33]. The original study employed a Metropolis-driven Kawasaki Hamiltonian[32] with local exchange and stationary polaron distributions. This approach reproduced the observed suppression of phase separation under sufficiently high illumination. However, to more accurately reproduce the temporal evolution of the phase separation observed in the experiments, we extended this framework in several aspects. First, we included a constantly updating polaron distribution. Second, we separated hole and electron contributions, allowing both to have different interaction strengths. Third, holes and electrons can each be adjusted to accumulate at either bromide-rich or iodide-rich

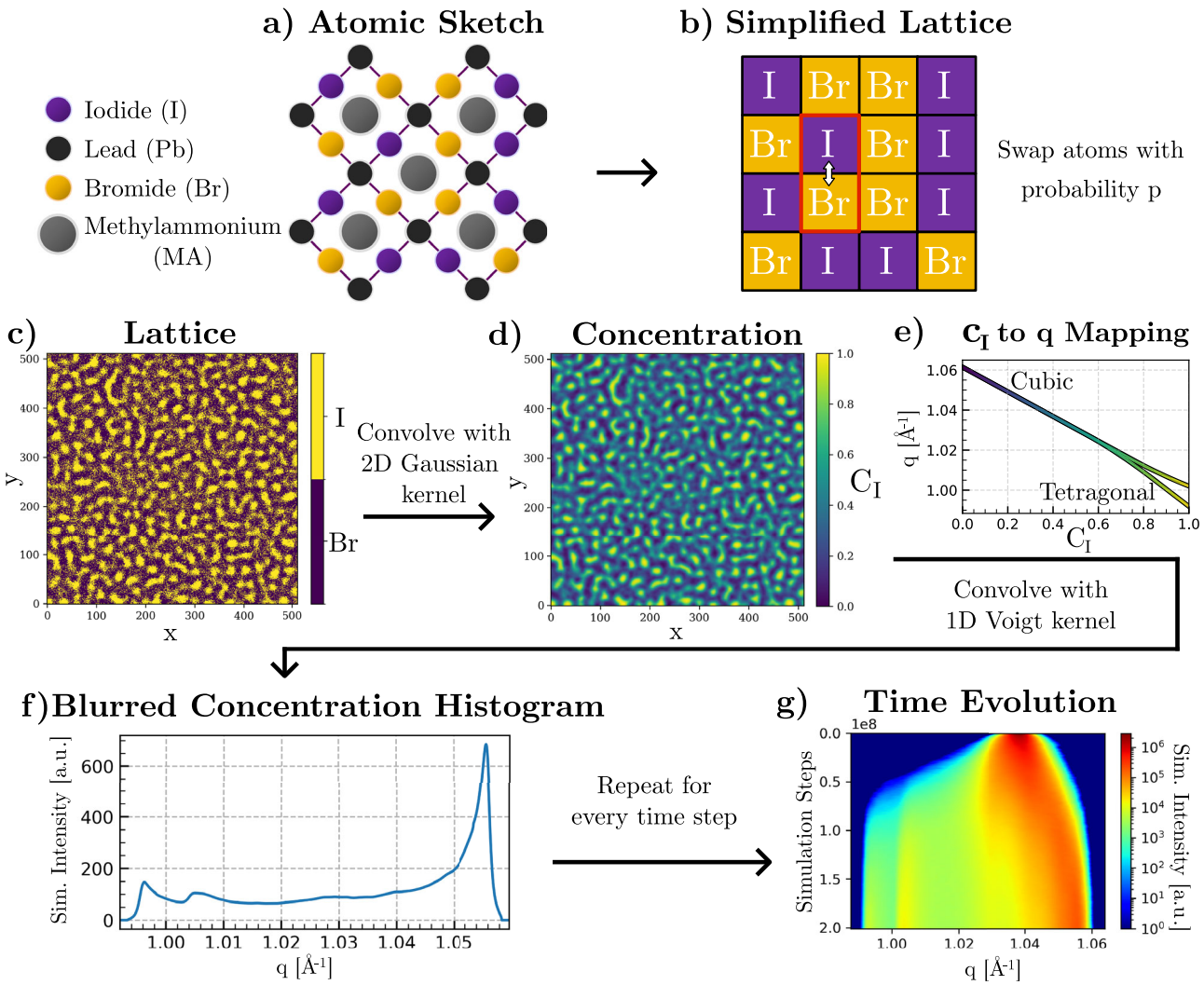



**Fig. 4 | Overview of the simulation pipeline, from lattice construction to synthetic diffraction data. a** Atomic sketch of perovskite structure. **b** Simplified halide sublattice of a perovskite structure, together with an indicated swap. The swap is accepted with probability $p$. **c** Example of a phase-separated lattice $\Lambda$ with iodide and bromide. **d** Concentration matrix obtained by convolution of the lattice $\Lambda$ shown in (**c**) with a 2D Gaussian kernel. **e** Relation between the iodide concentration $C_I$ and the $q$-position of the 001 diffraction peaks for cubic and tetragonal crystal structures of the mixed LHPs. **f** Histogram of the converted concentration matrix $C_I$ shown in (**d**), which was further blurred by convolution with a 1D Voigt kernel. **g** Time evolution of the blurred histogram (**f**) shown against the number of simulation steps. The lattice panels (**c**, **d**) use a square example lattice.

regions, independently of one another. Finally, we introduced a gradient to the polaron probability distribution along the $y$-axis to simulate the gradual absorption of light within a thick perovskite film (see Supplementary Information).

As previously stated, the MC simulation operates on a matrix $\Lambda$ consisting of $+1$ (iodide) and $-1$ (bromide), representing a lattice with iodide and bromide species respectively (Figure 4b). The updating mechanism, to simulate intra-lattice diffusion, follows the Metropolis algorithm with periodic boundary conditions. At each step, a random lattice site and one of its four nearest neighbours are selected. A new state is then generated in which these two selected sites are swapped. The energies of the initial and the swapped state are calculated, and a random number $0 \le r \le 1$ is generated. The swapped state is accepted if:

$$r < e^{-(\Delta E + E_B)/T} \tag{2}$$

$$\Delta E = H_S - H_I \tag{3}$$

where $\Delta E$ is the energy difference, $H$ is the Hamiltonian of any given state ($H_S$ - swapped state, $H_I$ - initial state), $E_B$ is the energy barrier that needs to be overcome and $T$ is the temperature. Throughout, reduced units are used, with $k_B = 1$, and all energy-related quantities, including $T$ and $E_B$, are expressed in these units.

To calculate the energy of any state we use a modified version of the Kawasaki Hamiltonian from Mao et al.[33]

$$H = \sum_{\langle i,j \rangle} J_{ij} \Lambda_i \Lambda_j - c_h \sum_{i=1}^{N} h_i^h \Lambda_i - c_e \sum_{i=1}^{N} h_i^e \Lambda_i \tag{4}$$

Here $\Lambda_i$ corresponds to the lattice value at location $i$, $N$ is the total number of lattice sites, $J_{ij} > 0$ controls the strength of the mixing term and is given in reduced units. Furthermore, $J_{ij}$ scales as the inverse square of the distance $d_{ij}$ between atom $i$ and $j$ ($J_{ij} = J/d_{ij}^2$). $\langle i, j \rangle$ denotes that the sum runs over neighbouring site pairs for which $d_{ij} \le 2a$, where $a$ is the lattice parameter. The absolute values of the parameters $c_h$ and $c_e$ define the strength of the hole and electron interaction (also using reduced units), while their signs control which halide species are energetically attracted to polaron-rich regions: a positive value attracts iodide (and repels bromide),

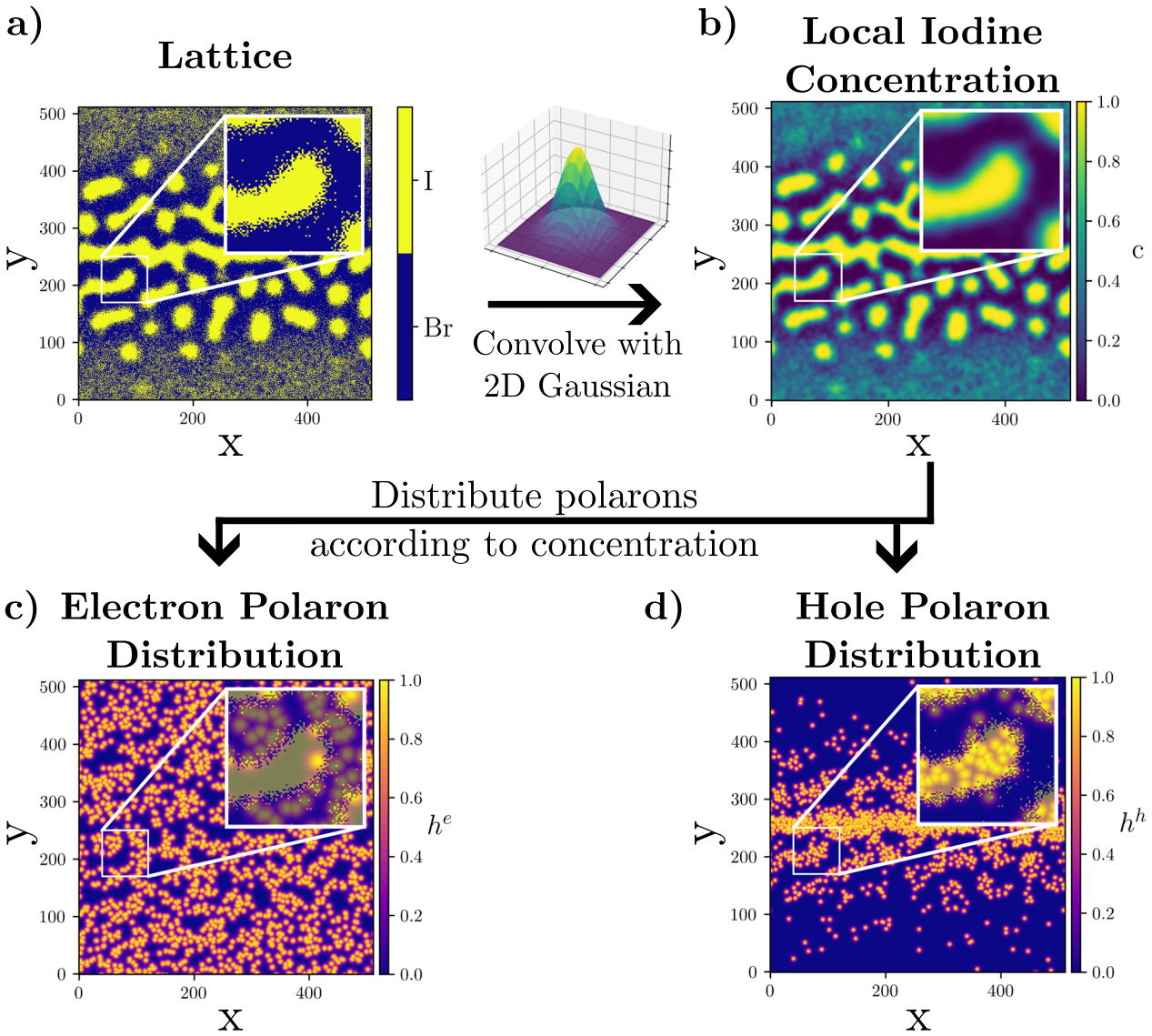



**Fig. 5 | Example of the polaron fields $h^e$ and $h^h$ generation process. a** Exemplary phase-separated lattice. Yellow pixels correspond to iodide species and blue pixels to bromide species. **b** Lattice from (**a**) convolved with a 2D Gaussian function with the variance $\sigma_c^2$ resulting in the iodide concentration matrix $C_I$. **c**, **d** Randomly generated electron- and hole-polaron distribution. The polaron gradients ($g_h = 2 \times 10^{-2}$, $g_e = 10^{-4}$) are set to more extreme values than those used in the main simulation ($g_h = 5 \times 10^{-3}$, $g_e = 10^{-3}$) to better show the parameter's effect. The inset plot shows an overlay of the strength of the polaron field with the concentration $C_I$, where hole-polarons accumulate within regions of high iodide concentration $C_I$, and electron-polarons accumulate within regions of high bromide concentration $C_{Br}$.

while a negative value attracts bromide (and repels iodide). Finally, $h_i^h$ and $h_i^e$ represent the hole- and electron-polaron-field strength at lattice site $i$.

The first term of this Hamiltonian favours mixing of the halide species and is always non-zero. Since the polaron terms are negligible in the dark, this mixing term dominates there, so the ground state of the model in the dark is the mixed state. The last two terms are contributions of the electron- and hole-polarons, which scale with the polaron number and therefore become significant only under illumination, remaining negligible in the dark. Both terms drive the phase separation by making the demixed state energetically more favourable. Here we consider them separately, as opposed to the previous work[33], where a single common term accounted for their contribution. This separation is physically motivated by the distinct band curvatures of the conduction and valence bands[10], which yield different effective masses and correspondingly different Fröhlich coupling constants for electrons and holes[34], and by the asymmetric band alignment between the iodide- and bromide-rich phases, implying different energetic driving forces per carrier species. Collapsing both contributions into a single term would suppress these asymmetries and prevent systematic testing of which carrier accumulation configuration is consistent with the measured dynamics.

The polaron distribution is coupled to the local halide concentration because free charge carriers locally distort the lattice, inducing stress and altering the energy landscape. Polarons respond to these changes much faster than ions can diffuse[56], and therefore relax first by minimising this local lattice distortion. Because lattice distortions are linked to internal electric fields that depend on the electronic structure and bonding characteristics of the different halide species, the energetic cost of distortion varies locally. Consequently, polarons tend to accumulate near atomic species for which the lattice distortion, and associated energy penalty, is smallest.

To generate the polaron-fields $h^h$ and $h^e$, the concentration matrix $C_I$ as well as $C_{Br} = 1 - C_I$ are used (Fig. 5a, b). Here, $C_I$ is computed using Eq. (1) with standard deviation $\sigma_{c,p}$, which sets the spatial range over which the local halide concentration influences the polaron accumulation probability. To

**Table 1 | Simulation parameters**

| Parameter | Value | Physical Description |
|---|---|---|
| *Lattice & Simulation Timing* | | |
| Lattice shape ($N_x \times N_y$) | 500 × 706 | Dimensionality of the simulated grid (Width × Height). |
| Total simulation steps | $1.25 \times 10^{10}$ | Total attempted Monte Carlo swaps. |
| Initial equilibration | $2.5 \times 10^9$ | Warm-up steps to reach steady state. |
| Polaron Update Rate ($\tau_{pol}$) | 25,000 | Every time $\tau_{pol}$ steps are taken the polaron field is updated. |
| *Illumination Protocol* | | |
| Light-on duration | $5 \times 10^9$ | Steps under constant illumination. |
| Light-off duration | $5 \times 10^9$ | Relaxation steps in dark. |
| *Polaron Densities* | | |
| Light-on polarons ($N_{on}$) | 5,000 | Steady-state photogenerated carriers per species. |
| Light-off polarons ($N_{off}$) | 100 | Residual polaron count per species. |
| *Polaron Locations* | | |
| Hole location | *Iodide* | Holes accumulate within iodide-rich regions. |
| Electron location | *Bromide* | Electrons accumulate within bromide-rich regions. |
| *Interaction & Transport Properties* | | |
| Interaction strengths ($c_h$, $c_e$) | 20, − 75 | Species-specific polaron-field coupling constants. |
| Mixing parameter ($J$) | 8 | Strength of the electronic mixing term. |
| Temperature ($T$) | 3 | Acceptance probability control. |
| Energy barrier ($E_B$) | 18 | Threshold for successful swap. |
| Concentration blurring width diffraction ($\sigma_{c,q}$) | 6 | Range of lattice parameter response to halide composition. |
| Concentration blurring width polaron ($\sigma_{c,p}$) | 6 | Range of polaron localisation relative to halide concentration. |
| Polaron sizes ($\sigma_h$, $\sigma_e$) | 3, 4 | Gaussian polaron sizes. |
| Gradient strengths ($g_h$, $g_e$) | $5 \times 10^{-3}$, $10^{-3}$ | Polaron distribution gradients. |

The simulation shown in Figure 2 uses these values for its lattice kinetics and polaron interactions.
All energetic parameters ($J$, $c_e$, $c_h$, $E_B$, $T$) are presented in reduced units. All length parameters (Lattice shape, $\sigma_{c,q}$, $\sigma_{c,p}$, $\sigma_h$, $\sigma_e$) are given in lattice parameter units $a$, while the gradient prefactors $g_h$ and $g_e$ are given in $1/a$.

obtain a more realistic probability distribution for thick films, a gradient along the $y$-direction (out-of-plane) was introduced to account for the gradual attenuation of light and the differing mobilities of electron- and hole-polarons[34].

The polaron density maximum is placed at the centre of the lattice ($y = N_y/2$, where $N_y$ is the number of lattice sites along the out-of-plane $y$ direction) and decays symmetrically towards both boundaries (see Figure 5c, d), so that $y = 0$ and $y = N_y$ experience equal intensity. This maximum represents the illuminated surface. In a real film the light enters at one surface and decays with depth, which would place the brightest region at a lattice edge and create a discontinuity under periodic boundary conditions. To avoid this, the film is mirrored about its illuminated surface: the two surfaces meet at the centre of the lattice, so each half represents one physical film, brightest at the centre and decaying towards the edge. The final probability distribution is obtained by multiplying this gradient with the concentration matrix:

$$P(x,\, y) = C(x,\, y) \cdot \exp\left(-\left|y - \frac{N_y}{2}\right| \cdot g_{h/e}\right) \tag{5}$$

Here, $P$ is the probability weight matrix for electrons or holes to be at specific lattice sites. $C$ is the local concentration of the halide species at which the given polaron type preferentially accumulates; $N_y$ is the number of cells in the $y$ direction, and $g_{h/e}$ is the gradient pre-factor.

The entries of the matrix $P$ are then used as probability weights to distribute a set number of polarons across the lattice. The electrons and holes can each be chosen to accumulate at high iodide or high bromide concentration, yielding the corresponding probability matrices $P_I$ and $P_{Br}$ from Eq. (5). Each polaron-field $h_i^h$ and $h_i^e$ at the lattice site $i$ (Eq. (4)) is defined according to a Gaussian distribution with width $\sigma_e$ for electron polarons and $\sigma_h$ for hole polarons around the centre of the polaron, normalised to a range of [0, 1] (Figure 5c, d).

If several polarons overlap at a lattice site, the largest value is taken as the local polaron-field strength, ensuring the field remains bounded between 0 and 1 while preserving a non-zero gradient throughout the lattice. The polaron-field is then updated every $\tau_{pol}$ simulation steps.

The resulting Monte Carlo simulation framework was used to generate the example simulation shown in Figure 2. The simulation parameters, summarised in Table 1, were determined from a combination of direct measurements, theoretical derivations, literature values, and iterative optimisation; details of each are provided in the Supplementary Information. The simulation was implemented in Python (version 3.13.5), using NumPy and SciPy; the full environment specification is provided with the deposited code.

The simulation was initiated with a low dark-state polaron count below the phase separation threshold, representing thermal carrier generation and weak ambient illumination. This ensured that the system remained in the mixed state during initialisation, consistent with the experimentally observed illumination threshold for phase separation[5,41], and allowed the initially random lattice to relax into its mixed steady state prior to the main illumination period. The polaron count was then increased to simulate illumination and drive phase separation, before being reduced to this dark-state value to allow recovery into the mixed state.

Since each polaron species (electrons and holes) could independently accumulate at either iodide- or bromide-rich regions, there are four physically distinct combinations to consider. To determine which of these reproduces the experimental observations, we simulated all four scenarios keeping all other parameters fixed at the values in Table 1, so that the resulting differences in Figure 3 isolate the effect of the polaron accumulation sites.

## Data availability

The X-ray diffraction data recorded at DESY are available at https://doi.org/10.60883/ddca671b81. All other data measured, generated, and analysed during the current study are available from the corresponding author upon reasonable request.

## Code availability

The simulation code that supports the findings of this study is openly available in the Zenodo repository at https://doi.org/10.5281/zenodo.20643267.

Received: 7 July 2026; Accepted: 8 September 2026;
Published online: 06 November 2026

## References

1. Schmidt-Mende, L. et al. Roadmap on organic-inorganic hybrid perovskite semiconductors and devices. *APL Mater.* **9**, 109202 https://doi.org/10.1063/5.0047616 (2021).
2. Zhang, L. et al. Advances in the application of perovskite materials. *Nano-Micro Lett.* **15**, 177 https://doi.org/10.1007/s40820-023-01140-3 (2023).
3. Zhang, L. et al. Diverse perovskite solar cells: Progress, challenges, and perspectives. *Adv. Mater.* **38**, e12221 https://doi.org/10.1002/adma.202512221 (2026).
4. Huang, H. et al. Growth mechanism of strongly emitting $CH_3NH_3PbBr_3$ perovskite nanocrystals with a tunable bandgap. *Nat. Commun.* **8**, 996 https://doi.org/10.1038/s41467-017-00929-2 (2017).
5. Wang, Y. et al. Phase segregation in inorganic mixed-halide perovskites: from phenomena to mechanisms. *Photon. Res.* **8**, A56–A71 https://doi.org/10.1364/PRJ.402411 (2020).
6. Zheng, X., Chen, B., Wu, C. & Priya, S. Room temperature fabrication of $CH_3NH_3PbBr_3$ by anti-solvent assisted crystallization approach for perovskite solar cells with fast response and small j-v hysteresis. *Nano Energy* **17**, 269–278 https://doi.org/10.1016/j.nanoen.2015.08.023 (2015).
7. Konstantakou, M., Perganti, D., Falaras, P. & Stergiopoulos, T. Anti-solvent crystallization strategies for highly efficient perovskite solar cells. *Crystals* **7**, 291 (2017).
8. Boyd, C., Cheacharoen, R., Leijtens, T. & McGehee, M. D. Understanding degradation mechanisms and improving stability of perovskite photovoltaics. *Chem. Rev.* **119**, 3418–3451 https://doi.org/10.1021/acs.chemrev.8b00336 (2019).
9. Manser, J. S., Saidaminov, M. I., Christians, J. A., Bakr, O. M. & Kamat, P. V. Making and breaking of lead halide perovskites. *Acc. Chem. Res.* **49**, 330–338 https://doi.org/10.1021/acs.accounts.5b00455 (2016).
10. Tao, S. et al. Absolute energy level positions in tin- and lead-based halide perovskites. *Nat. Commun.* **10**, 2560 https://doi.org/10.1038/s41467-019-10468-7 (2019).
11. Brennan, M. C., Ruth, A., Kamat, P. V. & Kuno, M. Photoinduced anion segregation in mixed halide perovskites. *Trends Chem.* **2**, 282–301 https://doi.org/10.1016/j.trechm.2020.01.010 (2020).
12. Noh, J. H., Im, S. H., Heo, J. H., Mandal, T. N. & Seok, S. I. Chemical management for colorful, efficient, and stable inorganic-organic hybrid nanostructured solar cells. *Nano Lett.* **13**, 1764–1769 https://doi.org/10.1021/nl400349b (2013).
13. Anaya, M., Lozano, G., Calvo, M. E. & Míguez, H. $ABX_3$ perovskites for tandem solar cells. *Joule* **1**, 769–793 https://doi.org/10.1016/j.joule.2017.09.017 (2017).
14. Hoke, E. T. et al. Reversible photo-induced trap formation in mixed-halide hybrid perovskites for photovoltaics. *Chem. Sci.* **6**, 613–617 https://doi.org/10.1039/C4SC03141E (2015).
15. Barker, A. J. et al. Defect-assisted photoinduced halide segregation in mixed-halide perovskite thin films. *ACS Energy Lett.* **2**, 1416–1424 https://doi.org/10.1021/acsenergylett.7b00282 (2017).
16. Bischak, C. G. et al. Origin of reversible photoinduced phase separation in hybrid perovskites. *Nano Lett.* **17**, 1028–1033 https://doi.org/10.1021/acs.nanolett.6b04453 (2017).
17. Knight, A. J. et al. Electronic traps and phase segregation in lead mixed-halide perovskite. *ACS Energy Lett.* **4**, 75–84 https://doi.org/10.1021/acsenergylett.8b02002 (2018).
18. Maschwitz, T. et al. How crystallization additives govern halide perovskite grain growth. *Nat. Commun.* **16**, 9894 https://doi.org/10.1038/s41467-025-65484-7 (2025).
19. Knight, A. J. & Herz, L. M. Preventing phase segregation in mixed-halide perovskites: a perspective. *Energy Environ. Sci.* **13**, 2024–2046 https://doi.org/10.1039/D0EE00788A (2020).
20. Sebastian, S. et al. Additive screening for suppressing light-induced phase segregation and ionic activity in halide perovskite devices. *ACS Appl. Mater. Interfaces* **17**, 57335–57342 https://doi.org/10.1021/acsami.5c08005 (2025).
21. Datta, K. et al. Light-induced halide segregation in 2D and quasi-2D mixed-halide perovskites. *ACS Energy Lett.* **8**, 1662–1670 https://doi.org/10.1021/acsenergylett.3c00160 (2023).
22. Shao, Y. et al. Grain boundary dominated ion migration in polycrystalline organic-inorganic halide perovskite films. *Energy Environ. Sci.* **9**, 1752–1759 https://doi.org/10.1039/C6EE00413J (2016).
23. Yun, J. S. et al. Critical role of grain boundaries for ion migration in formamidinium and methylammonium lead halide perovskite solar cells. *Adv. Energy Mater.* **6**, 1600330 https://doi.org/10.1002/aenm.201600330 (2016).
24. Niu, T. et al. Stable high-performance perovskite solar cells via grain boundary passivation. *Adv. Mater.* **30**, 1706576 https://doi.org/10.1002/adma.201706576 (2018).
25. Wu, J. et al. Strain in perovskite solar cells: origins, impacts and regulation. *Natl. Sci. Rev.* **8**, nwab047 https://doi.org/10.1093/nsr/nwab047 (2021).
26. Gualdrón-Reyes, A. F. et al. Controlling the phase segregation in mixed halide perovskites through nanocrystal size. *ACS Energy Lett.* **4**, 54–62 https://doi.org/10.1021/acsenergylett.8b02207 (2019).
27. Hu, L. et al. Linking phase segregation and photovoltaic performance of mixed-halide perovskite films through grain size engineering. *ACS Energy Lett.* **6**, 1649–1658 https://doi.org/10.1021/acsenergylett.1c00213 (2021).
28. Haddadi Barzoki, F., Griesbach, M., Köhler, A. & Grüninger, H. Finite size effects on light-induced correlated ionic and electronic transport in mixed halide perovskites. *ACS Energy Lett.* **11**, 2829–2840 https://doi.org/10.1021/acsenergylett.5c04123 (2026).
29. Tian, L., Xue, J. & Wang, R. Halide segregation in mixed halide perovskites: Visualization and mechanisms. *Electronics* **11**, 700 (2022).
30. Kerner, R. A., Xu, Z., Larson, B. W. & Rand, B. P. The role of halide oxidation in perovskite halide phase separation. *Joule* **5**, 2273–2295 https://doi.org/10.1016/j.joule.2021.07.011 (2021).
31. Lilly, J. R. S. et al. Is photoluminescence spectroscopy a suitable probe of halide segregation? *ACS Energy Lett.* **11**, 3953–3961 https://doi.org/10.1021/acsenergylett.6c00432 (2026).
32. Kawasaki, K. Kinetics of Ising models. in *Phase Transitions and Critical Phenomena* (eds Domb, C. & Green, M.S.) Vol. 2, 443–501 (Academic Press, 1972).
33. Mao, W. et al. Light-induced reversal of ion segregation in mixed-halide perovskites. *Nat. Mater.* **20**, 55–61 https://doi.org/10.1038/s41563-020-00826-y (2021).
34. Miyata, K. et al. Large polarons in lead halide perovskites. *Sci. Adv.* **3**, e1701217 https://doi.org/10.1126/sciadv.1701217 (2017).
35. Jin, Z. et al. Photoinduced large polaron transport and dynamics in organic-inorganic hybrid lead halide perovskite with terahertz probes. *Light Sci. Appl.* **11**, 209 https://doi.org/10.1038/s41377-022-00872-y (2022).

36. Steele, J. A. et al. How to GIWAXS: Grazing incidence wide angle X-ray scattering applied to metal halide perovskite thin films. *Adv. Energy Mater.* **13**, 2300760 https://doi.org/10.1002/aenm.202300760 (2023).
37. Dubey, M., Turedi, B., Kanak, A., Kovalenko, M. V. & Leite, M. S. Reversible, photo-induced lattice distortions in halide perovskites. *Adv. Mater*. e21800 https://doi.org/10.1002/adma.202521800 (2026).
38. Tsai, H. et al. Light-induced lattice expansion leads to high-efficiency perovskite solar cells. *Science* **360**, 67–70, https://doi.org/10.1126/science.aap8671 (2018).
39. Rolston, N. et al. Comment on "light-induced lattice expansion leads to high-efficiency perovskite solar cells". *Science* **368**, 8691 https://doi.org/10.1126/science.aay8691 (2020).
40. Vegard, L. Die Konstitution der Mischkristalle und die Raumfüllung der Atome. *Z. Phys.* **5**, 17–26 https://doi.org/10.1007/BF01349680 (1921).
41. Draguta, S. et al. Rationalizing the light-induced phase separation of mixed halide organic-inorganic perovskites. *Nat. Commun.* **8**, 200. https://doi.org/10.1038/s41467-017-00284-2 (2017).
42. Wright, A. D., Patel, J. B., Johnston, M. B. & Herz, L. M. Temperature-dependent reversal of phase segregation in mixed-halide perovskites. *Adv. Mater.* **35**, 2210834 https://doi.org/10.1002/adma.202210834 (2023).
43. Lehmann, F. et al. The phase diagram of a mixed halide (Br, I) hybrid perovskite obtained by synchrotron X-ray diffraction. *RSC Adv.* **9**, 11151–11159 https://doi.org/10.1039/C8RA09398A (2019).
44. Cahn, J. W. & Hilliard, J. E. Free energy of a nonuniform system. I. Interfacial free energy. *J. Chem. Phys.* **28**, 258–267 https://doi.org/10.1063/1.1744102 (1958).
45. Muscarella, L. A. et al. Lattice compression increases the activation barrier for phase segregation in mixed-halide perovskites. *ACS Energy Lett.* **5**, 3152–3158 https://doi.org/10.1021/acsenergylett.0c01474 (2020).
46. Motti, S. G. et al. Phase segregation in mixed-halide perovskites affects charge-carrier dynamics while preserving mobility. *Nat. Commun.* **12**, 6955 https://doi.org/10.1038/s41467-021-26930-4 (2021).
47. Merten, L. et al. Halide segregated crystallization of mixed-halide perovskites revealed by in situ GIWAXS. *ACS Appl. Mater. Interfaces* **16**, 8913–8921 https://doi.org/10.1021/acsami.3c18623 (2024).
48. Fassl, P. et al. Fractional deviations in precursor stoichiometry dictate the properties, performance and stability of perovskite photovoltaic devices. *Energy Environ. Sci.* **11**, 3380–3391 https://doi.org/10.1039/C8EE01136B (2018).
49. Fassl, P. et al. Effect of density of surface defects on photoluminescence properties in $MAPbI_3$ perovskite films. *J. Mater. Chem. C.* **7**, 5285–5292 https://doi.org/10.1039/C8TC05998E (2019).
50. Falk, L. M. et al. Effect of precursor stoichiometry on the performance and stability of $MAPbBr_3$ photovoltaic devices. *Energy Technol.* **8**, 1900737 https://doi.org/10.1002/ente.201900737 (2020).
51. Greco, A. et al. Kinetics of ion-exchange reactions in hybrid organic-inorganic perovskite thin films studied by in situ real-time X-ray scattering. *J. Phys. Chem. Lett.* **9**, 6750–6754 https://doi.org/10.1021/acs.jpclett.8b02916 (2018).
52. Kneschaurek, E. et al. Compact sample environment for in situ X-ray scattering during spin-coating. *Rev. Sci. Instrum.* **94**, 063901 https://doi.org/10.1063/5.0149613 (2023).
53. Nakamura, Y. et al. Crystal systems and lattice parameters of $CH_3NH_3Pb(I_{1-x}Br_x)_3$ determined using single crystals: validity of Vegard's law. *Inorg. Chem.* **59**, 6709–6716 https://doi.org/10.1021/acs.inorgchem.9b03421 (2020).
54. Abukaev, A. et al. *pygid*: a Python package for fast data reduction in grazing-incidence diffraction. *J. Appl. Crystallogr.* **59**, 263–275 https://doi.org/10.1107/S1600576725010593 (2026).
55. Eames, C. et al. Ionic transport in hybrid lead iodide perovskite solar cells. *Nat. Commun.* **6**, 7497 https://doi.org/10.1038/ncomms8497 (2015).
56. Meggiolaro, D., Ambrosio, F., Mosconi, E., Mahata, A. & De Angelis, F. Polarons in metal halide perovskites. *Adv. Energy Mater.* **10**, 1902748 https://doi.org/10.1002/aenm.201902748 (2020).


## Acknowledgements

We acknowledge DESY (Hamburg, Germany), a member of the Helmholtz Association HGF, for the provision of experimental facilities. Parts of this research were carried out at PETRA III at the beamline P10. Beamtime was allocated for proposal I-20220787. Computational resources were provided in part by the Maxwell HPC Cluster (DESY). We thank the LISA+ facility at the University of Tübingen for their support. Furthermore, we thank Prof. Dr. M. Oettel, who assisted in the interpretation of the simulations. Financial support was provided via DAPHNE4NFDI (German Research Foundation DFG project 460248799). We thank the Cluster of Excellence – Machine Learning for Science, funded by the DFG under Germany's Excellence Strategy (EXC No. 2064/1, project No. 390727645), for support and access to computer resources. We acknowledge the OSCARS project, which has received funding from the European Commission's Horizon Europe Research and Innovation programme under grant agreement No. 101129751. The research was partially funded by the Federal Ministry of Education and Research (BMBF) and the Baden-Württemberg Ministry of Science as part of the Excellence Strategy of the German Federal and State Governments. We acknowledge support from the Open Access Publication Fund of the University of Tübingen.

## Author contributions

Conceptualisation: S.S., I.Z. and F.S.; Sample preparation: Y.V. and F.P.; Experiment: S.S., I.Z., E.K., D.L., H.M., N.S., P.Z., A.H., F.U. and F.W.; Data analysis and simulation: S.S.; Supervision: I.Z. and F.S.; the manuscript was written by S.S. with contributions from all authors.

## Funding

Open Access funding enabled and organized by Projekt DEAL.

## Competing interests

The authors declare no competing interests.

## Additional information

**Supplementary information** The online version contains supplementary material available at https://doi.org/10.1038/s41524-026-02334-0.

**Correspondence** and requests for materials should be addressed to Ivan Zaluzhnyy or Frank Schreiber.

**Reprints and permissions information** is available at http://www.nature.com/reprints

**Publisher's note** Springer Nature remains neutral with regard to jurisdictional claims in published maps and institutional affiliations.

**Open Access** This article is licensed under a Creative Commons Attribution 4.0 International License, which permits use, sharing, adaptation, distribution and reproduction in any medium or format, as long as you give appropriate credit to the original author(s) and the source, provide a link to the Creative Commons licence, and indicate if changes were made. The images or other third party material in this article are included in the article's Creative Commons licence, unless indicated otherwise in a credit line to the material. If material is not included in the article's Creative Commons licence and your intended use is not permitted by statutory regulation or exceeds the permitted use, you will need to obtain permission directly from the copyright holder. To view a copy of this licence, visit http://creativecommons.org/licenses/by/4.0/.

© The Author(s) 2026